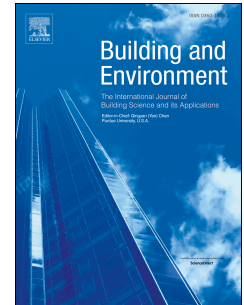# Accepted Manuscript

Outdoor measurement of wall pressure on cubical scale model affected by atmospheric turbulent flow

C. Hirose, N. Ikegaya, A. Hagishima, J. Tanimoto

Please cite this article as: Hirose C, Ikegaya N, Hagishima A, Tanimoto J, Outdoor measurement of wall pressure on cubical scale model affected by atmospheric turbulent flow, *Building and Environment* (2019), doi: https://doi.org/10.1016/j.buildenv.2019.106170.

1 Title:

2 Outdoor measurement of wall pressure on cubical scale model affected by atmospheric

3 turbulent flow

4

5 Authors:

6 C. Hirose[1], N. Ikegaya[1], A. Hagishima[1], and J. Tanimoto[1]

7

8 Affiliations:

9 [1]Interdisciplinary Graduate School of Engineering Sciences, Kyushu University, Japan

10

11 Corresponding author:

12 C. Hirose

13 Kasuga-koen 6-1, Kasuga-shi, Fukuoka 816-8580, Japan

14 Phone/Fax: +81-92-583-7644

15 Email: chiyoko_ikgy@kyudai.jp

16

17 Abstract:

18 Most studies on indoor ventilation have utilized wind-tunnel experiments (WTEs) or
19 computational fluid dynamics based approaches under well-controlled flow conditions.
20 However, the effects of urban boundary layer flow with variable wind directions and various
21 turbulence scales on the ventilation driven by the pressure differences between the upwind
22 and downwind sides of a building within a block array is still under discussion. Therefore, we
23 conducted outdoor experiments at comprehensive outdoor scale model (COSMO) experiment
24 sites in an urban climate to clarify the relationships between the building wall pressure
25 differences and the approaching flow. The pressure coefficients for the outdoor site were
26 comparable with those obtained during previous WTEs. Accordingly, temporal variations in
27 the wind speed and pressure coefficient on the target block were investigated in detail using
28 low-pass filtering operations. The relationships between the filtered wind speed and the
29 pressure differences indicate that the slower temporal variations in the wall pressure showed
30 good agreement with the filtered approaching flow. In addition, the correlation coefficient
31 between the filtered wind speed and the wall pressure differences quantified the apparent
32 coherence between the turbulent flow and the ventilation rate. Furthermore, the statistics of
33 the ventilation rate were determined based on the conventional model to clarify the effects of
34 the turbulent flow on the natural ventilation rate. The ratios between the mean and short-term
35 ventilation rates imply that the short-term ventilation rate presented dramatic temporal
36 fluctuations owing to the various scale turbulence generated by the atmospheric flow.

37

38 Highlights:

39 Simultaneous outdoor measurements of atmospheric flow and wall pressure on a cube

40 Temporal variations of filtered wind speed and wall pressure are obviously correlated

41 Correlation between wind speed and wall pressure increases with filtering period

42 Short-term ventilation rate indicates dramatic variations in natural ventilation

43

44 Keywords:

45 Comprehensive outdoor scale model experiment; Natural ventilation; Wind pressure

46 coefficient; Urban boundary layer

47

48

49

50   1. Introduction
51   Wind-induced natural ventilation is driven by the pressure difference between two
52   walls through openings and is commonly used as a low-energy ventilation method. In addition,
53   the occupants of naturally ventilated rooms tend to be satisfied with the indoor environment
54   despite the higher temperature and CO_2 concentration compared to mechanically ventilated
55   rooms, as reported by Hummelgaard et al. [1]. In contrast, accurate estimations of the natural
56   ventilation rates are required to maintain clean indoor air and to provide thermal comfort for
57   the occupants.
58   In general, to estimate the natural ventilation rates of a building, the conventional
59   method of macroscopic approximation is employed under the assumption of steady-state flow
60   conditions. The method predicts the ventilation flow rate Q [m^3/s] based on Bernoulli's
61   principle using the wall pressure differences Δp between two building faces, as expressed by
62   Eq. (1-1).

$$Q = \alpha A \sqrt{\frac{2\Delta p}{\rho}} \tag{1-1}$$

63   ere, αA indicates the effective opening area and ρ [kg/m^3] is the air density. To
64   understand the features of Δp, various studies using both wind-tunnel experiments (WTEs)
65   and computational fluid dynamics (CFD) approaches have been conducted on simplified
66   building shapes (e.g., Marshall [2] and Ohba et al.[3] for WTE, Seifert et al. [4] and Asfour et
67   al. [5] for CFD). In addition, the applicability of the macroscopic model was investigated by
68   comparing the ventilation rates determined using the model with those obtained using a
69   numerical simulation of the indoor air coupled with outdoor flow fields (e.g., Seifert et al. [4],
70   Asfour et al. [5]). Moreover, coupled simulations of indoor and outdoor airflows have been
71   conducted by Peren et al. [6] and Peren et al. [7] to identify that subtle shape changes, such as
72   opening positions or small eaves on openings, could increase cross ventilation rates.
73   Although these previous studies clarified the importance of building conditions,
74   accurately estimating the natural ventilation of a building within urban areas may be
75   considerably difficult because of various influential factors, such as the arrangement of the
76   surrounding buildings, the packing density of building arrays, and the shape of the target
77   building. Therefore, the effect of neighboring buildings on the ventilation rate has been
78   considered. Cheng et al. [8] and Zaki et al. [9] reported that the Δp values for buildings
79   within urban-like arrays monotonically decreased as the block packing ratio increased, owing
80   to the sheltering effect of the surrounding blocks. In addition, Kim et al. [10] revealed that the
81   mean pressure coefficient similarly decreased, whereas the turbulent pressure coefficient
82   increased owing to turbulence generation by the surrounding blocks. Furthermore, Ikegaya et
83   al. [11] noted that the cumulative ventilation rate of a block within an urban-like array became
84   comparable with the mean ventilation rate. However, the short-term ventilation rate varied
85   temporally, and instantly yielded to the drastically weaker or stronger ventilation conditions.
86   Moreover, Cheung and Liu [12] discussed the effects of the surrounding buildings for various
87   approaching wind directions. Similarly, Murakami et al. [13] estimated the presence of three
88   types of ventilation rates (net, gross, and instantaneous) for various opening positions of a
89   building in block arrays. In addition to these studies on the effect of surrounding block models
90   on Δp, it is well known that the indoor flow structures of the target block sheltered by
91   surrounding block arrays were found to be altered by neighboring buildings and their layout
92   (Tominaga and Blocken [14], Ikegaya et al. [15]).
93   Further to these flow characteristics determined by the building scale, some recent
94   urban climatology studies have also shown the existence of outdoor turbulent flow structures.
95   Kanda [16] reported that turbulent organized structures, which might extend up to ten times

2

96   the size of buildings, developed over urban building arrays. Obviously, such larger-scale
97   turbulent motion would influence the wind-driven natural ventilation because these structures
98   cause high-speed downward and low-speed upward flows, which are known as sweep and
99   ejection events, respectively, as reported by Castro et al. [17] and Michioka et al. [18].
100   Therefore, to understand the wind-induced ventilation in urban areas, it is important to
101   evaluate how such urban turbulence affects the temporal variation and special distribution of
102   building wall pressure.

103   In most previous studies employing WTEs or CFD regarding building ventilation, the
104   flow conditions, such as the wind speed, direction, and turbulence intensity, were well
105   controlled. In contrast, the interactions between the indoor ventilation and the outdoor
106   turbulent flows must be considered. Under the circumstances, there have only been a few
107   studies on the temporal variations of natural ventilation under atmospheric flow conditions
108   (Gough et al. [19], King et al. [20], Gough et al. [21]). Gough et al. [19] conducted outdoor
109   experiments to clarify the influence of surrounding blocks and turbulence of various
110   timescales on ventilation. In addition, King et al. [20] performed numerical simulations to
111   identify the effect of the wind direction on ventilation. However, studies on the natural
112   ventilation of a building in a realistic atmospheric urban boundary layer are still scarce.

113   We have conducted outdoor experiments at the comprehensive outdoor scale model
114   (COSMO) facility to clarify the relationships between the building wall pressure and realistic
115   atmospheric turbulent flow over urban-like block arrays. Section 2 explains the experimental
116   setup and conditions; Section 3 describes the observed atmospheric conditions and mean
117   pressure distribution; Section 4 discusses how the turbulent flow and Δp values correlate; and
118   conclusive remarks are presented in Section 5.

119   2. Experimental methodology

120   2.1 Field measurement experiments

121   Experiments were conducted at the COSMO experiment site at the Nippon Institute
122 of Technology in Saitama, Japan (139º42' east longitude and 36º01' north latitude). The
123 details of the COSMO site have been minutely described by Inagaki et al. [22]. The COSMO
124 site comprises 512 cubical blocks with the height H = 1.5 m, which is 1/5 of the size of
125 typical residential buildings in Japan. The site features a 100×50 m^2 concrete foundation.
126 The surroundings of the site were grassland and paddy field. The cubical scale models are
127 arranged in a lattice-type square pattern with the packing density λ_p = 25% (Fig. 1(a)). The
128 site was employed by various previous studies on outdoor scale-model experiments (e.g.
129 Inagaki et al. [22], Kanda and Moriizumi [23], Inagaki and Kanda [24], Takimoto et al. [25]).

130   The measurements were conducted from 3:00 pm on the 14th to 7:00 pm on the 16th
131 of May, 2016. During this period, the southeastern (SE) wind occurred more frequently than
132 the northwestern (NW) wind owing to the transition of seasons from spring to summer,
133 although the prevailing wind direction at the site was confirmed to be NW in winter and SE in
134 summer (Fig. 1 (b)). These directions are along the longer sides of the COSMO site. The
135 details of the experimental conditions during the measurement periods are described in
136 Section 3.1. The red square in Fig. 1(a) represents the target block used to determine the Δp
137 values and was located 4 rows and 12 columns from the southwestern (SW) and NW edges of
138 the site. Although other equipment was installed on site, the location of the experiments was
139 carefully selected. The position of the target block was at least 10 rows from the edge of the
140 site or the location of the sun shade, which covers the block cubes in most parts of the SE half
141 of the site (illustrated in Fig. 1(a) as fractal sun shade). The effects of the wind direction due
142 to the upwind sun shade are discussed in Section 3.2.

143   As illustrated in Fig. 1(c), the streamwise velocity, u, is the velocity of the NW wind
144 along the longitudinal direction of the site, and v and w are the spanwise and vertical wind
145 velocities, respectively. The horizontal wind direction, θ, ranged from -180° to 180°.

146

147

148

4
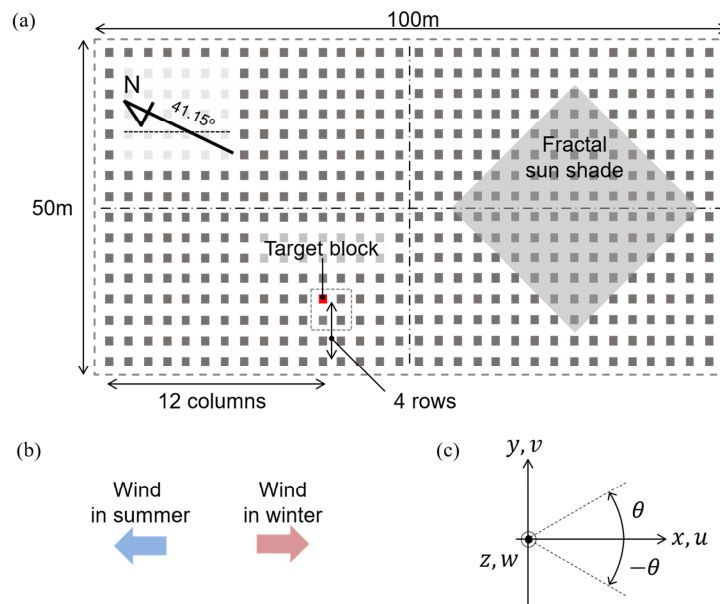
(d)

Fig 1. (a) Plan for the COSMO site, (b) anticipated prevailing wind direction for each season, (c) coordinate system defined for field measurements, and (d) photograph of the COSMO site taken from the east side. The target block is located 4 rows and 12 columns from the SW and NW edges of the site, respectively. The number of blocks upwind of the target block exceeded 10 for both the SE and NW wind directions. The horizontal wind direction, θ, ranged from -180° to 180°.

2.2 Measurement details of wind speed and wall pressure

Fig. 2(a) depicts the apparatus used to measure the velocity over the target block and the pressure on the block sides. To measure the three velocity components over the target block, we installed a SONIC, DA-700 sonic anemometer (sampling at 10 Hz, error on u ±0.005 [m/s]) equipped with a TR90-T probe at a height of $0.5H$ from the top of the target block. In addition to the sonic anemometer, 10 mm thick acrylic plates featuring pressure taps 3.2 mm in diameter were installed on both the NW and SE sides of the target block using 40 mm wide aluminum frames, which were screwed onto the cubical target block. Therefore, the actual length of the block in the streamwise direction became 1.6 m (frame width: 0.04 m, acrylic plate thickness: 0.01 m for both sides, and the total thickness of the frame and plate: 0.1 m), whereas the height was 1.5 m. Aluminum tubes 20 mm in length were inserted into each hole on the acrylic plate and were connected to silicon tubes. The outside faces of the acrylic plate and aluminum tubes were carefully adjusted to be identical. The void spaces created between the plates and the block faces were used to install the silicon tubes connected to the taps. The tubes were gathered together and connected to OKANO, DPC-500N12 pressure manometers (sampling at 10 Hz, error on p ±0.1 [Pa]), which were placed in a container located next to the target block. The dimensions of the container were approximately $0.5 \times 0.4 \times 0.3$ m^3. Although the container could have slightly affected the air flow between the blocks, it was necessary to position it there to avoid the response delay of the pressure manometers, which depended on the length of the tubes between the pressure taps and the sensors. Fig. 2(b) illustrates the detailed positions where the wall pressure was measured. Positions 1–5 and 6–10 were located near the edge and at the center line of the block face, respectively. Each pressure manometer measured the pressure differences between the NW and SE block faces at each position: $\Delta p = p_{NW} - p_{SE}$. The pressure differences were simultaneously measured at five different locations on the block faces using five manometers. Both the pressure and wind speed values were collected using a GRAPHTECH, GL7000 data logger with a frequency of 10 Hz. Except for the pressure manometers, all devices were placed in containers located two blocks away from the target block.

The measurements were conducted under dry conditions to avoid water entering the tubes from the pressure taps. Two sets of trials with no missing data were gathered: CASE1 for 26.9 h with measurements at positions 1-5 and CASE2 for 6.0 h with measurements at positions 6-10 (Fig. 2(b)).
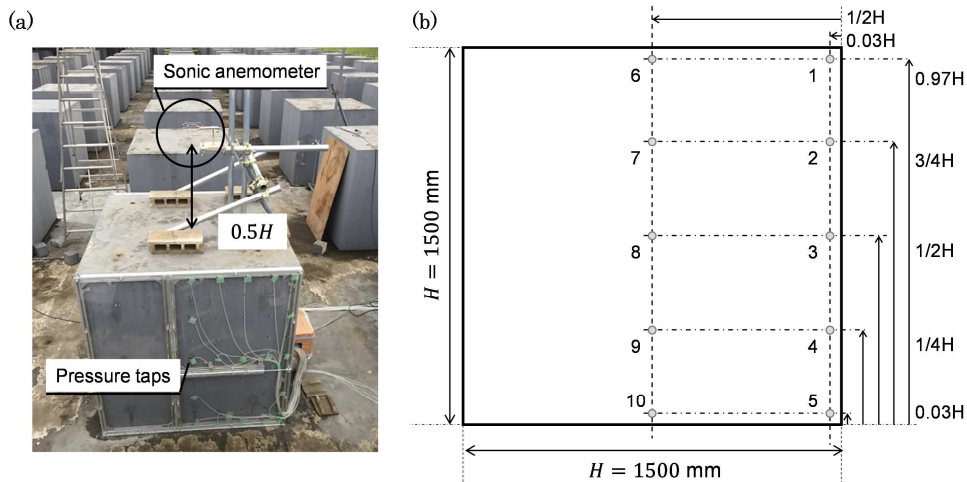
191   Fig 2. Measurement apparatus installation: (a) sonic anemometer position and pressure tap
192   plates location on target block and (b) positions of pressure measurement taps on block faces.
193   H = 1500 mm is the height of the cubical block.

194   3. Temporally averaged statistics
195   3.1 Approaching flow conditions
196   We examined the probability distributions of u and the horizontal wind direction
197   measured at $0.5H$ above the top of the block for CASE1 and CASE2 (Fig. 3). Table 1
198   summarizes several velocity data for each trial: magnitude of the mean streamwise velocity,
199     $|U|$, standard deviation of u, σ_u, maximum and minimum u values, u_{max} and u_{min},
200   respectively, and occurrence frequency of the NW and SE winds ($|\theta| < 15°$ and $|\theta| > 165°$,
201   respectively). We were able to determine that the stronger SE wind occurred more frequently
202   than the NW wind during both trials. As listed in Table 1, the occurrence frequencies of the
203   NW wind were 30% and 46.5% for CASE1 and CASE2, respectively, whereas those of the
204   SE wind were 10.6% and 0.5%, respectively. Thus, it was concluded that the wind came from
205   both directions for CASE1, even though the frequency of the NW wind was lower than that of
206   the SE wind. Therefore, the effect of the upwind sun shade at the COSMO site was analyzed
207   based on the measurement data for CASE1 (see Section 3.2). In contrast with CASE1, the
208   NW wind rarely manifested during the CASE2 trial. The Reynolds number of the block
209   height became $Re_H = UH/\nu \approx 1.1–1.6 \times 10^5$, where ν [m²/s] is the kinematic viscosity.
210   In addition, the expected roughness Reynolds number, which can be calculated using the
211   following formula: $Re^* = u^* z_o/\nu$, where u^* [m/s] is the friction velocity (derived from
212     $u^* = U\sqrt{0.5C_d}$, where C_d is the drag coefficient that can be estimated by $C_d \cong 1.2 \times 10^{-2}$,
213   as shown in Hagishima et al. [26]) and z_o [m] is the roughness length (estimated to be $z_o =$
214     $0.1H$ as followed by Macdonald et al. [27]), was certainly larger than O(1) for the employed
215   outdoor scale model under the specified wind speed conditions. Therefore, the fully rough
216   conditions, where the turbulence flows within and near the canopy satisfies the scale
217   similarity, were achieved (Snyder and Castro [28]) owing to the large scale of the outdoor
218   experiment compared to those of WTEs, although the mean wind speed range was
219   approximately 1 m/s. This enabled the comparison between the outdoor experimental data in
220   this study and previous experimental data (e.g., Zaki et al. [29] and Cheng and Castro [30]) or
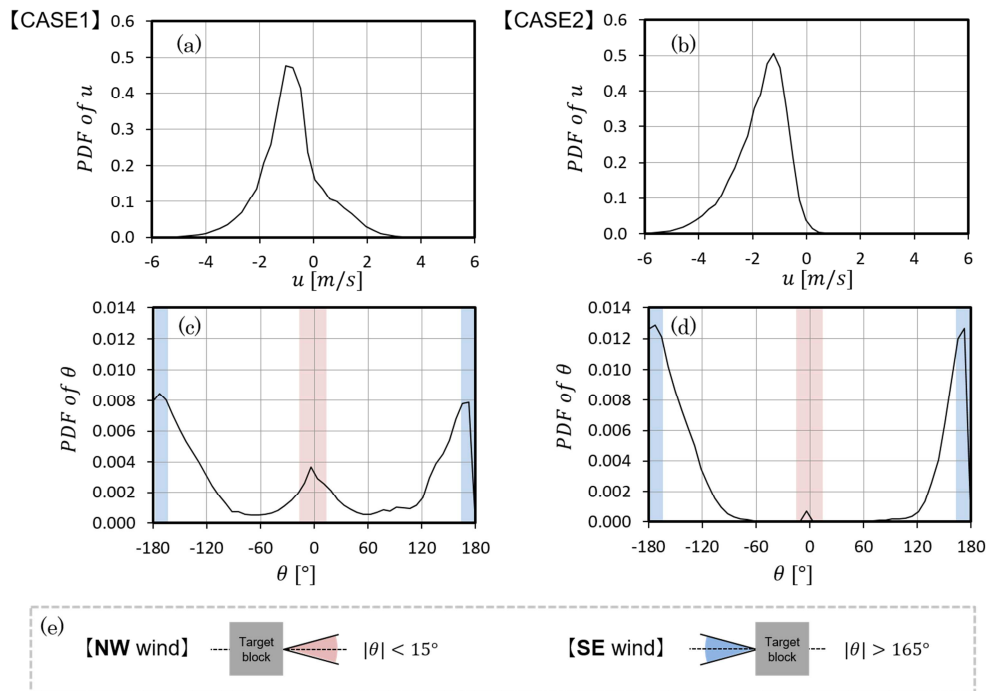221   computational scale model results (e.g., Coceal et al. [31]).
222
223

224

225 Fig. 3. Probability density functions (PDFs) for horizontal wind speed u for (a) CASE1 and
226 (b) CASE2 and for horizontal wind direction θ for (c) CASE1 and (d) CASE2. (e)
227 Definitions of SE and NW winds. The blue and red shaded areas in (c) and (d) represent the
228 wind directions for the apparent NW and SE winds ($|\theta| < 15°$ and $|\theta| > 165°$, respectively).
229
230

231 Table 1. Approaching flow conditions measured at $0.5H$ above the target block on the
232 COSMO site: magnitude of mean streamwise velocity, $|U|$ (± 0.005 [m/s]), standard deviation
233 of streamwise velocity, σ_u (± 0.005 [m/s]), occurrence frequency of apparent NW and
234 apparent SE winds, Reynolds number of the block height, Re_H, expected roughness Reynolds
235 number, Re^*, and measurement period for CASE1 and CASE2.
236

	CASE 1	CASE 2
$|U|$ [m/s]	1.07 (± 0.005)	1.61 (± 0.005)
σ_u [m/s]	0.95 (± 0.005)	0.39 (± 0.005)
Frequency of NW wind [%] ($|\theta| < 15^o$)	10.6	0.5
Frequency of SE wind [%] ($|\theta| > 165^o$)	30.0	46.5
$Re_H = HU/\nu$	1.1×10^5	1.6×10^5
$Re^* = z_o u^*/\nu$	8.2×10^2	1.2×10^3
Measurement period [hour]	26.9	6.0

237

238   3.2 Relationships between u and Δp

239   The relationships between u and Δp were examined, as illustrated in Figs. 4(a)–(e)
240   for CASE1 and Figs. 4(f)–(j) for CASE2. The u and Δp raw data were averaged for 10 min.
241   The averaging period of 10 min was selected to be a shorter timescale than the spectral gap of
242   the power spectral density of the streamwise velocity to reduce large-scale fluctuations. The
243   plots in Fig. 4 are distinguished between the apparent NW wind (positive u, $|\theta| < 15°$), and
244   the apparent SE wind (negative u, $|\theta| > 165°$). As can be seen in Fig. 4(a), the magnitude of
245   Δp at position 1 (Fig. 2(b)) clearly increased as the magnitude of u increased. The tendency
246   of Δp to increase as u increased gradually weakened for the lower measurement positions,
247   as can be seen in Figs. 4(b)–(e). These trends were plausible because the dynamic pressure
248   attributed to the approaching flow became weaker for the lower positions. Moreover, the data
249   for the lower positions were more scattered than those for the upper positions. This occurred
250   because it was difficult to accurately detect dynamic pressure values smaller than 0.5 Pa using
251   pressure manometers, although the employed one was able to detect pressure differences with
252   the accuracy of 0.1 Pa. In addition, the wind directions at the $1.5H$ and lower positions
253   might differ because of the three-dimensional flows within the canopy layer owing to the
254   block arrays, which caused discrepancies in the approaching flow directions between the
255   lower measurement positions and those above the block. Similar tendencies were observed for
256   CASE2, as illustrated in Figs. 4(f)–(j). That is, the large appreciation of pressure occurred at
257   position 6, which was at the top and center of the block face, and the gradient of the pressure
258   differences with respect to the wind speed gradually decreased for the lower positions.
259   Moreover, the plots for the lower positions analyzed in the CASE1 trial were scattered. For
260   the CASE2 trial, NW winds were not recorded during the 10 min intervals used to measure
261   the averaged wind speeds; therefore, no data was available in the positive u value range.

262   In addition to such tendencies, we were able to recognize that these trends did not
263   vary even though the data were restricted according to the wind directions of the apparent NW
264   or SE winds, marked in Fig. 4 using square and circular symbols, respectively. Thus, the
265   horizontal wind directions did not affect the Δp values between the target block faces if u,
266   which was normal to the block faces, was considered to be the influential approaching wind
267   speed. According to these results, more investigations on the relationships between u and Δp
268   were conducted using the data obtained for all wind directions (see Section 3.4).

269   Based on the plots of u and Δp, the pressure coefficients, C_p, were determined as
270   follows. In steady-state conditions, the relationship between the approaching wind speed and
271   Δp can be expressed using C_p:

$$\Delta p = 0.5\rho u^2 C_p. \tag{3-1}$$

272   The C_p values for each position were derived using the least square method. The solid,
273   dashed red, and dashed blue lines in Fig. 4 represent the regressed lines derived from Eq.
274   (3-1), where the deduced C_p values were based on all data, the apparent NW wind, and the
275   apparent SE wind, respectively. For the CASE2 trial, there were no apparent NW wind
276   conditions; therefore, only the plots for all data and apparent SE wind are depicted. The
277   differences in the three lines for CASE1 in Figs. 4(a)–(e) are subtle, and they indicate that the
278   C_p values for both wind directions were very similar. Therefore, the effect of the upwind sun
279   shade on the block cubes from most areas of the SE half side of the testing site (see Section
280   2.1) were negligible under SE wind conditions owing to the sufficient fetch consisting of the
281   block arrays. In addition, the consistent tendencies between the dashed lines (regressed line
282   for the apparent wind directions) and solid lines (regressed line for all data) confirmed the
283   aforementioned hypothesis that u only influenced Δp. Although subtle deflections of the
284   dashed and solid lines can be observed for the lower positions 3 and 4, these might have

10

285 occurred due to the difficulties in measuring the small values of the pressure differences for
286 the lower positions as well as the complex flow generation within the deep canopy height.
287 According to these results, both trials were considered to further analyze the relationships
288 between Δp on the target block and approaching turbulent flows generated by the cubical
289 block array.

290

291

292

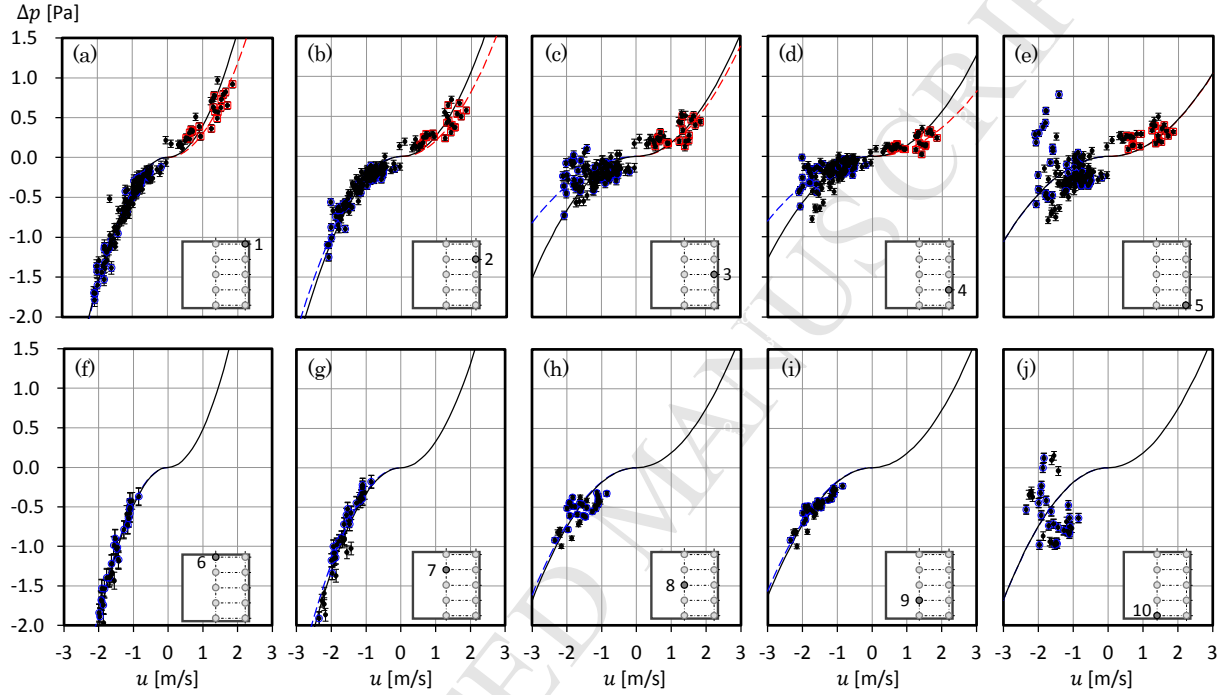| Wind direction	Measurement	Equation
All	●	——
SE wind ($|\theta| < 15°$)	○	- - -
NW wind ($|\theta| < 165°$)	□	- - -

293
294 Fig. 4. Relationships between wall pressure difference, Δp, and streamwise velocity, u, at a
295 height of $1.5H$. The Δp and u values were averaged for 10 min: (a)–(e) results for positions
296 1–5 (CASE1) and (f)–(j) results for positions 6–10 (CASE2). The solid line represents the
297 $\Delta p = 0.5\rho u^2 C_p$ plot, where the deduced pressure coefficient, C_p, is based on all data, and
298 the dashed red and blue lines represent the $\Delta p = 0.5\rho u^2 C_p$ plots for the NW and SE winds,
299 respectively. Error bars indicate measurement accuracies of the pressure manometers (0.1 Pa).

11

3.3 Comparison of C_p values

Fig. 5(a) illustrates the vertical distributions of the C_p values between block faces at the center line (positions 6–10, CASE2) and at the edge line (positions 1–5, CASE1). The error bars indicate the standard deviations of the pressure coefficients. The C_p values increased as the height increased for the upper half positions of the block faces, whereas the values remained nearly constant for the lower half positions. In addition, the C_p value at the edge was larger than those at the center for the upper half positions. Since the block array was lattice-square type and its packing density was $\lambda_p = 25\%$, a stable vortex with very low wind speed might be generated in the cavities between two blocks and the approaching flows over the blocks might only skim the air at the upper parts of the cavity (which is known as the skimming flow regime, Oke [32]). Additionally, the velocity in the street areas, where no obstacles were present in the streamwise direction, remained larger. Consequently, the dynamic pressure on the block faces increased only for the upper half of the cavity. Furthermore, the dynamic pressure values near the block edge increased.

In Fig. 5(b), the averaged C_p values at the center and near the edge of the block were compared with the spanwise-averaged ones obtained from WTEs conducted by Zaki et al. [29] for different λ_p values, and were scaled using the average C_p values on block faces. The reported data were intermediate between those obtained for λ_p values of 8% and 31% during WTEs, indicating the transition of the C_p values owing to the increase in λ_p was consistent with the results of the WTEs. These comparisons ensured that consistent vertical distributions of the C_p values were obtained even though the measurement scale was considerably different from that of the WTEs. Although the consistency was plausible because of the sufficiently large Reynolds number conditions for the outdoor measurements in this study, it is interesting to note that the large-scale variations in wind speed and direction did not affect the C_p values of the block in the average sense.
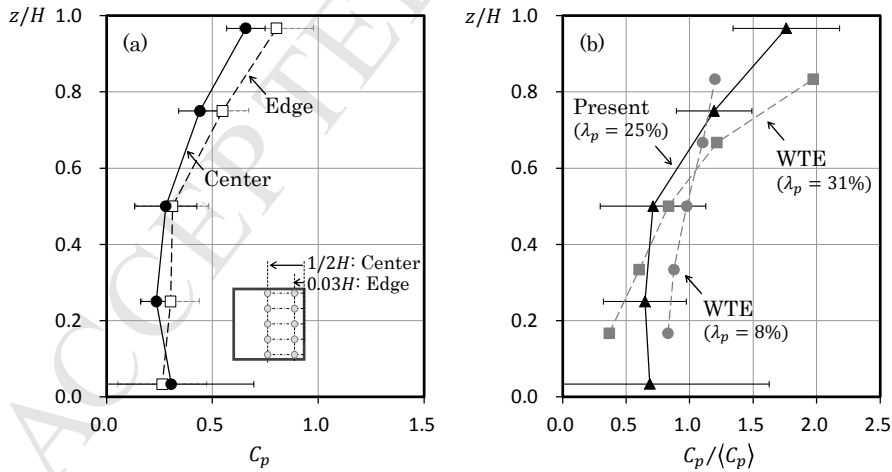

Fig. 5. (a) Pressure coefficients, C_p, at the center and near-edge of the block determined using the least-squares method using Eq. (3-1). (b) Vertical distribution of $C_p/\langle C_p \rangle$ compared with data from WTEs conducted by Zaki et al. [29]. $\langle C_p \rangle$ is the average C_p for all measurement positions on the block face and λ_p is the packing density for each condition. Error bars represent the standard deviations of C_p.

333   4. Temporal variations

334   4.1 Temporal distribution of filtered wind speed and C_p

335   This section describes the temporal variations in u above the block and Δp to

336   examine the instantaneous pressure-driven ventilation induced by the turbulence of the

337   approaching air flow. For the conventional macroscopic model, the ventilation rate Q [m/s^3]

338   was calculated using Eq. (1-1). Therefore, the pressure difference operating as ventilation

339   potential should be temporally averaged during a certain period T [s]. A variable featuring

340   overbar and capital T (i.e., $\overline{\phi}^T$) represents the filtered value of the variable, ϕ, for a certain

341   period T, as described by the following equation:

$$\overline{\phi}^T (t) = \frac{1}{T} \int_{-T/2}^{T/2} \phi(t - \tau) d\tau \tag{4-1}$$

342   Based on Eq. (4-1), the raw data for any variable, ϕ, is considered to be smoothed out by

343   applying a temporal low-pass filter for the filtering period of T. Therefore, the filtered

344   variable $\overline{\phi}^T$ can be considered to be the temporal variation of the variable in the absence of a

345   turbulence with frequency higher than $1/T$ [s^{-1}]. In other words, the time series data of the

346   filtered values of $\overline{\phi}^T (t)$ would vary according to the effects of the temporally longer- and

347   spatially larger-scale turbulences compared to those determined by the T period. Applying

348   the aforementioned filter operation to u and C_p, the relationships between u and Δp for

349   different timescales were examined. As the volume flow rate through a small opening could

350   be estimated using Eq. (1-1), as mentioned in Seifert et al. [3], the temporal variations of $\overline{C_{p_i}}^T$

351   correlated well with the expected temporary indoor ventilation changes attributed to the

352   turbulent flow near the block faces.

353   Figs. 6 and 7 illustrate the time series data in $\overline{u}^T$ and $\overline{C_{p_i}}^T$, where $\overline{C_{p_i}}^T =$

354    $\overline{\Delta p}^T /0.5\rho U^2$ for positions 1, 3, 5, 6, 8, and 10 on the block faces (we have omitted figures

355   for other positions because of the decreasing tendency of $\overline{C_{p_i}}^T$ with the measurement height.).

356   The subscript i represents the position number of the pressure tap, as illustrated in Fig. 2(b),

357   and U [m/s] is the absolute value of the mean streamwise velocity at a height of $1.5H$ for

358   the selected 2 h Four filters: t/t^*=1, 5, 10, and 100 were applied to confirm the differences

359   between the temporal variation patterns for different time scales. Here, t^* is defined as H/U,

360   and represents the estimated mean duration for an air parcel for the mean wind speed of U

361   [m/s] passing over a distance (or streamwise block length) of H [m]. The time-averaged

362   wind speed and C_p values for the selected 2 h are also depicted in Figs. 6 and 7 using dashed

363   lines.

364   The mean u value for the selected period in Figs. 6 and 7 was negative, indicating

365   that the flow direction was SE. As the pressure difference was defined as $\Delta p = p_{NW} - p_{SE}$,

366   the negative pressure difference values were caused by the larger dynamic pressure of the

367   approaching flow on the SE face of the block compared to that on the NW face of the block.

368   Comparing situations using different filter sizes (i.e., the gray and black lines in Figs. 6 and 7),

369   both the wind speed and C_p clearly indicated that the low-pass filtered values presented

370   smoother variation patterns because the turbulence smaller than T was eliminated. When

371   applying the same time filter, the overall coherences between the variations of the wind speed

372   and C_p at the top of the target block (i.e., positions 1 and 6) were clearer than those of the

373   lower positions (Figs. 6(a), (b), (e), and (f)). In addition, the amplitudes of C_p tended to be

374   the largest for those positions. Although the coherences between u and Δp weakened for the

375   lower positions (Figs. 6(d) and (h)), trends of temporal variations similar to those of u could

still be confirmed. These results indicate that the fluctuations in the wall pressure on the block were clearly affected by the turbulence of the approaching flow at each temporal filtering scale, when the dynamic pressure worked on the block faces.

In addition, we were able to confirm that the similarities in the appreciation and depreciation trends in the u and C_p values were more obvious as the filtering size increased. These results indicate that the longer time scale turbulence could cause more coherent and simultaneous variations in Δp at each position. This was probably due to the larger size of turbulence that caused the simultaneous changes in Δp on the wider areas of the block faces. Furthermore, the fluctuations in size of the shorter filter were more significant for the higher positions than for the lower ones (e.g., compared with Figs. 7(f)–(h)). This tendency also implies that the large turbulence size presented a more significant role in the pressure fluctuations near the lower level of the block, whereas the upper positions were significantly affected by small scale turbulence as well as large scale motions.

Although the temporal variations in Figs. 6 and 7 occurred during one of the episodes arbitrarily chosen from the entire measurement periods, the comparison of u and Δp qualitatively established the correlation between the air flow approaching the target block and the wall pressure on the block surfaces for a certain turbulence scale. The following section quantifies the relationship between u and Δp.
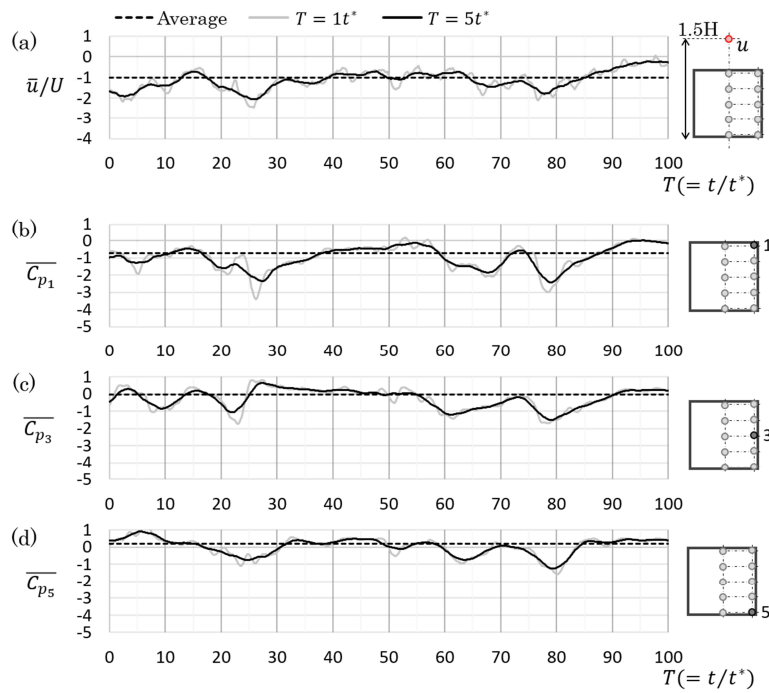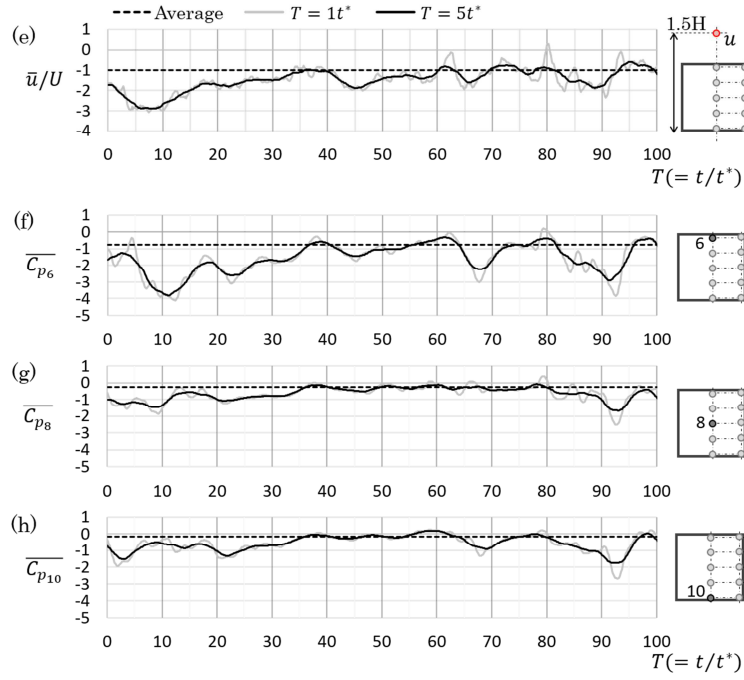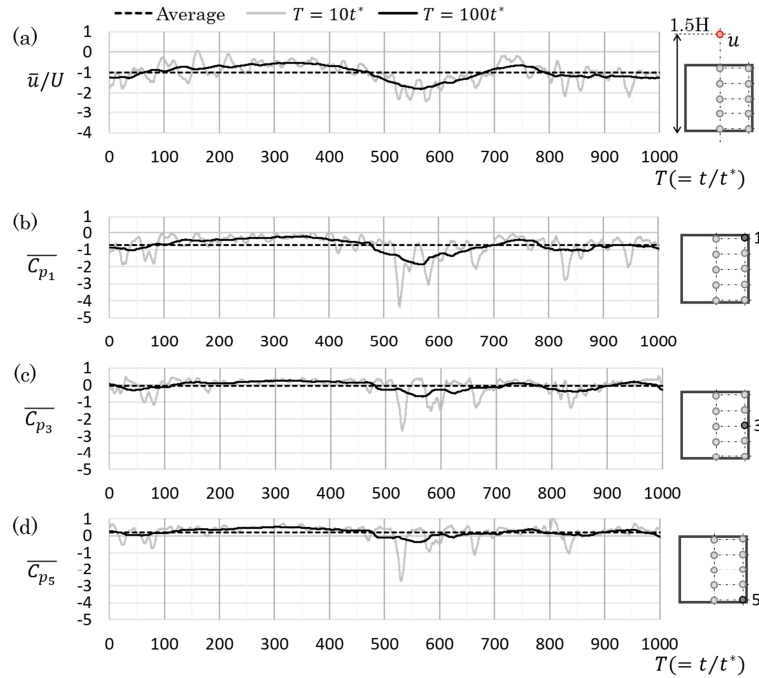
Fig. 6. Temporal variation of filtered variables for (a) streamwise velocity, $\overline{u}^T/U$ and (b)–(d) pressure coefficient, $\overline{C_{p_i}}^T$, at each position described in the schematics on the right side of each figure for CASE1; (e)–(h) are the equivalents of (a)–(d) for CASE2. The dotted lines represent the mean values for the selected 2 h. The gray and black lines indicate the temporal variation for the filtered periods of $1t^*$ and $5t^*$[s], respectively.
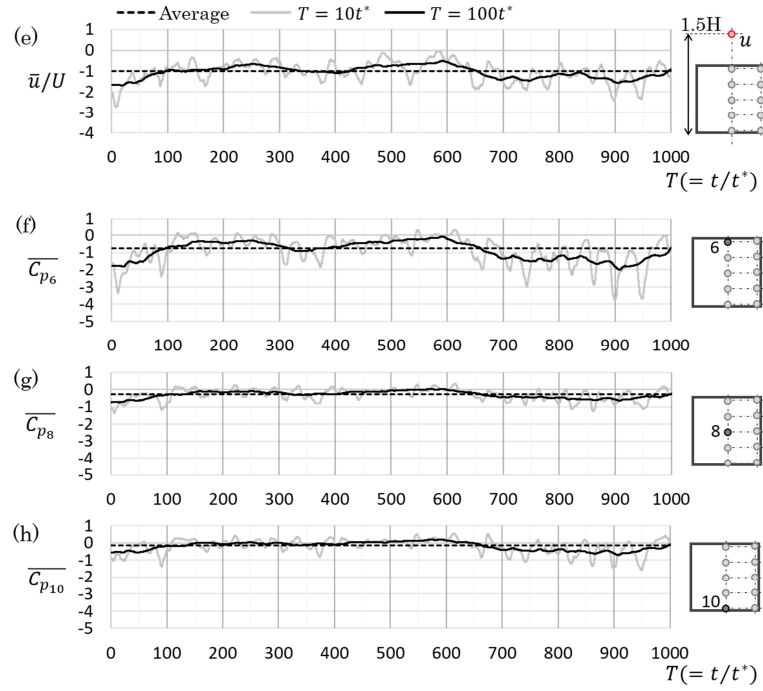

15

406
407 Fig. 7. Temporal variation of filtered variables for (a) streamwise velocity $\overline{u}^T/U$ and (b)–(d)
408 pressure coefficient $\overline{C_{p_i}}^T$ at each position described in the schematics on the right side of
409 each figure for CASE1; (e)–(h) are the equivalents of (a)–(d) for CASE2. The dotted lines
410 represent the mean values for the selected 2 h. The gray and black lines indicate the temporal
411 variation for the filtered periods of $10t^*$ and $100t^*$[s], respectively.

412 4.2. Quantification of relationship between u and Δp

413   For a more precise discussion on the coherence between u and Δp for different
414 timescales, the correlation coefficient between $\overline{u}^T$ and $\overline{\Delta p}^T$, $R_{u\Delta p_i}^T$, was calculated using Eq.
415 (4-2):

$$R_{u\Delta p_i}^T = \frac{\overline{\overline{u}^{T\prime} \overline{\Delta p_i}^{T\prime}}}{\sigma_{\overline{u}^T}\sigma_{\overline{\Delta p_i}^T}} \qquad (4\text{-}2)$$

416 where $\overline{u}^{T\prime}$ and $\overline{\Delta p_i}^{T\prime}$ are the temporal fluctuation (i.e., the differences between the averaged
417 filtered value for 2 h, $\overline{\overline{\phi}}^T$, and the filtered value, $\overline{\phi}^T$) of u and Δp, $\sigma_{\overline{u}^T}$ and $\sigma_{\overline{\Delta p_i}^T}$ are the

418 standard deviations calculated as $\sigma_{\overline{\phi}^T} = \left(\overline{(\overline{\phi}^T - \overline{\overline{\phi}}^T)^2} \right)^{0.5}$, and the overbar represents the

419 temporal average during the selected measurement period of 2 h.

420   The correlation coefficients for each filtering period are illustrated in Fig. 8. As
421 mentioned above, the longer the filtering period was, the stronger the correlation between u
422 and Δp was determined to be for all positions. In addition, the correlation coefficients for the
423 lower positions (i.e., positions 3, 5, 8, and 10) were significantly increased in accordance with
424 the length of the filtering period T. In contrast, the coherence between u and Δp for the top
425 positions presented lower sensitivity for the length of the filtering period T, namely, slight
426 increases in the correlation coefficients could be confirmed for positions 1 and 6. For example,
427 the increase rate of $R_{u\Delta p_1}^{100t^*} = 0.96$ and $R_{u\Delta p_1}^{1t^*} = 0.70$ for position 1 was 36%, whereas that
428 of $R_{u\Delta p_5}^{100t^*} = 0.83$ and $R_{u\Delta p_5}^{1t^*} = 0.39$ for position 5 was 112%. This small increase in $R_{u\Delta p_i}^T$
429 with T at positions 1 and 6 indicates that even small-scale turbulence significantly affected
430 the fluctuations in the wall pressure at the top of the block for the block-length scale of $1t^*$.
431 In contrast, such small-scale turbulence did not contribute to the Δp values for the lower
432 positions, and resulted in the significant increase in the correlation coefficient as the filtering
433 period increased. According to the mean flow structures around the cubical block array
434 presented in the numerical simulation reported by Coceal et al. [31], only the areas of the
435 block face near the top and side edges were exposed to strong approaching winds because of
436 the surrounding block arrays. At the same time, slow variations caused by the larger scale
437 turbulence, such as $10t^*$ and $100t^*$, also contributed to the wall pressure on the entire block
438 face. As a result, high-pressure areas could be observed near the edges on the block face (Fig.
439 5(a)).

440   The coherence between u and Δp on the center line (positions 8 and 10) was more
441 obvious than that on the edge line (positions 3 and 5) for any T value. This might be
442 explained by the well-known flow structures around the cubical block array. In general, a low
443 speed flow due to the stable vortex in the block cavity could be generated, as reported by
444 Coceal et al. [31
445]. In addition, the high-speed flow from the unobstructed channel region could penetrate
446 horizontally through the block cavity, as described by Ikegaya et al. [11]. Owing to these flow
447 structures, u at a height of $1.5H$ in the present study caused stronger coherence on the
448 center line than that on the edge line of the block because the stable vortex within the cavity
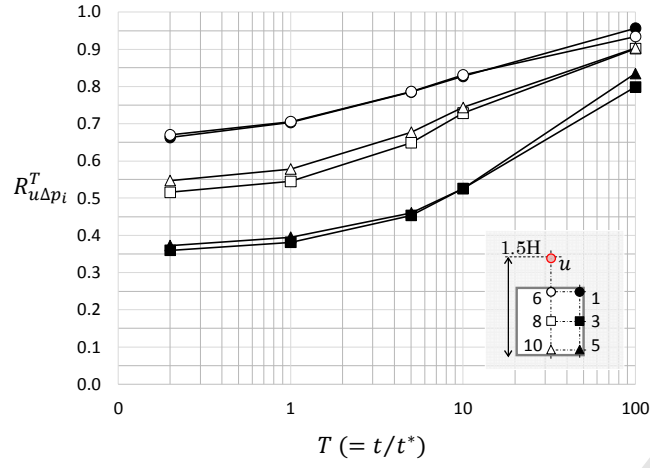449 was probably enhanced by the streamwise velocity over the block arrays.
450

451
452 Fig. 8. Correlation coefficient between the filtered streamwise wind speed and the wall
453 pressure differences, $R^T_{u\Delta p_i}$, defined by Eq. (4-2), for each filtering period T.

18

454   4.3 Temporal variations in expected ventilation rate

455   From the detailed analysis in the previous section, we concluded that the natural

456 ventilation driven by Δp must present temporal fluctuation caused by the unsteady

457 atmospheric flow around the target building. Therefore, in this section, we discuss the

458 temporal variations of the expected ventilation rate based on the $\overline{C_{p_i}}^T$ values at positions i,

459 for the averaging duration T.

460   As mentioned in Section 4.1, the pressure difference, Δp [Pa], between the

461 windward and leeward sides of the building is considered to be the driving force for the

462 wind-induced natural ventilation in a conventional macroscopic model for estimating the

463 building ventilation rate Q [m³/s]. Thus, based on Eq. (1-1), we could derive the relationship

464 between $\overline{\Delta p}^T$ [Pa] and ventilation rate, Q_T [m³/s], during a certain period T, as follows.

$$Q_T \propto \sqrt{\overline{\Delta p}^T} \qquad (4\text{-}3)$$

465 According to the definition of C_p (Eq. (3-1)), Q_T is proportional to $\overline{C_p}^T$ with a low-pass

466 temporal filter for the cut-off duration, T, as follows:

$$Q_T \propto \sqrt{\left|\overline{C_p}^T\right|} \qquad (4\text{-}4)$$

467 Using the method proposed by Ikegaya et al. [11], we defined Q_T as the short-term

468 ventilation rate because it indicated the temporally averaged ventilation rates during the

469 period T. In other words, Q_T represented the ventilation attributed to the turbulent effects

470 timescales larger than T. Accordingly, we were able to clarify the effects of turbulent flow in

471 the boundary layer on the mean ventilation rate by determining the ratio, $\beta(t)$, between $\overline{C_p}^T$

472 and the mean pressure coefficient, $\overline{C_p}$, for the total analysis time.

$$\beta(t) = \sqrt{\frac{|\overline{C_p}^T|}{|\overline{C_p}|}} \qquad (4\text{-}5)$$

473 Consequently, $\beta(t)$ satisfies the following relationship.

$$Q_T(t) = \beta(t)Q \qquad (4\text{-}6)$$

474 Therefore, the statistics of $\beta(t)$ in accordance with the filtering period, T, allowed us to

475 determine the statistical features of the short-term ventilation rate.

476   Fig. 9 illustrates the variations in β_i with the filtering duration $T(= t/t^*)$ for four

477 positions on the target block. The subscript i designates the measurement position. The black

478 lines and their error bars represent the average and standard deviations, respectively, the red

479 and blue lines are the maximum and minimum values, the red dotted and dashed lines

480 describe the 90th and 95th percentiles, and the blue dotted and dashed lines depict the 10th and

481 5th percentiles. Here, the N-th percentile indicates the lowest value with the occurrence

482 frequency of N%. We used the total analysis time of 7200 s (i.e., 72,000 sampling data), and

483 hence, β_i is unity when $t = 7200$ s, being equal to $t/t^* = 8261$ for CASE1 and

484 $t/t^* = 9006$ for CASE2.

485   As can be seen in Figs. 9(a) and (c), the mean values of β_1 and β_6 at the top height

486 of the block for the shortest filtering period are approximately 1; however, their standard

487 deviations are approximately 0.5. In addition, the 10th and 90th percentiles presented almost

488 comparable standard deviations ranges. In contrast, the maximum and minimum β_1 and β_6

489 values considerably differed from their corresponding mean values. These results indicate that

490 the temporally averaged short-term ventilation rate at the top height of the block can be

comparable with the mean ventilation rate. However, some extreme values may occur within the 0.4–1.3 or 0.2–1.8 times ranges of the mean ventilation rate at positions 1 and 6 (Figs. 9(a) and (c), respectively). In short, strong or weak ventilation could occur since the short-term ventilation rate, which depended on T, fluctuated temporally due to the large-scale variations in the approaching flow. In particular, the aforementioned tendency was more obvious at position 6 than at position 1. This might have occurred because of the typical flow patterns, such as both flows skimming over the blocks and blowing down the gaps between two blocks.

However, at the mid-height points of the target block (Figs. 9(b) and (d)), the standard deviations were larger than those at the top height. In particular, the increase in standard deviation at position 3 (Fig. 9(b)) was considerable. In addition, the mean value of β_3 became approximately 1.4, which indicated that the actual ventilation was stronger than that determined by the time averaged pressure coefficient. As can be seen in Fig. 5(a), the absolute values of C_p at the mid-height positions were smaller than that at top height because the mid-height positions were exposed to the relatively weak wind flow caused by the surrounding blocks. However, these positions were significantly affected by the large scale-turbulence flows in the channel and gaps of the series of blocks. Therefore, the short-term ventilation rate at position 3 was significantly different from its mean rate. Such underestimation of the ventilation rate compared to the short-term ventilating rate tended to be observed for the lower half positions of the block edge.

Therefore, we concluded that the ventilation rate could significantly change over the averaging time and with the position of the building wall because the variations in ventilation rate due to the various scales of turbulence were affected the by boundary layer as well as the surrounding building conditions.
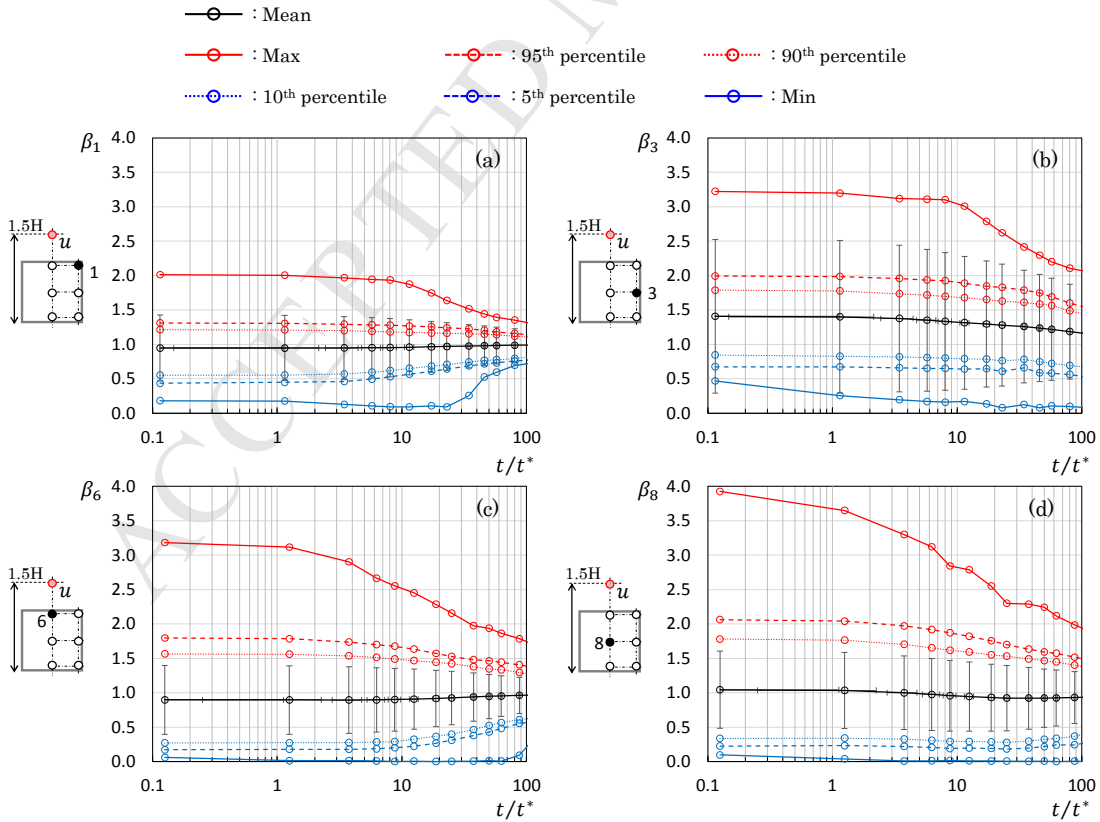

Fig. 9 Statistics of pressure coefficient ratios, β_i, for different filtering periods, T, at

519   positions (a) 1, (b) 3, (c) 6, and (d) 8. The subscripts i represent the position numbers of the
520   pressure taps illustrated in Fig. 2(b).

521   5. Conclusion

522   In this study, simultaneous measurements of atmospheric turbulent approaching flow
523   and Δp between the windward and leeward sides of the block were conducted at the COSMO
524   site. The relationships between the approaching flow and Δp were investigated under realistic
525   atmospheric conditions, such as varying wind speed, direction, and turbulence intensity, to
526   determine the temporal variations in wind-induced natural ventilation. The following
527   conclusions were drawn.

528   First, the C_p values of the outdoor site were comparable with the results obtained
529   during WTEs conducted by Zaki et al. [29], which justified the measurement techniques used
530   for the outdoor measurements in this study. In addition, no scale effect on the Δp was
531   observed, as expected. Second, the temporal variations in wind speed and C_p on the target
532   block were investigated in detail for several averaging periods by applying low-pass filtering
533   operation to both wind speed and Δp. The relationships between the filtered wind speed and
534   Δp indicated that the slower temporal variations in Δp had clearer coincidence with that of
535   approaching flow. This indicated that the ventilation rates of buildings immersed in the
536   realistic atmospheric boundary layer might temporally vary due to the temporal variations in
537   the approaching flow. The correlation coefficient between the filtered wind speed and Δp
538   quantitatively demonstrated the apparent coherence between turbulent flows and ventilation
539   rate.

540   In addition, the increasing trend in correlation coefficient with the filtering period
541   implied that slower variations in the approaching flow significantly affected the temporal
542   variations in Δp. Third, the statistics of the ventilation rate were determined based on the
543   conventional model to clarify the effects of turbulent flow on the natural ventilation rate. The
544   standard deviations and percentile values of the ratio between the mean and short-term
545   ventilation rates implied that the short-term ventilation rate exhibited significant temporal
546   fluctuations owing to the various scale of turbulence generated by the atmospheric flow. This
547   emphasized the importance of considering the short-term ventilation rate, which could
548   increase or decrease compared to the mean value, if the extreme ventilation rates become
549   problematic, such as evaluating the health risks of poisonous gases in factories or buildings
550   (sick building syndrome). Although we clarified the statistical relationships between the
551   atmospheric turbulent flow and Δp under real urban boundary conditions, there is still more
552   room for investigation for evaluating the effect of three-dimensional unsteady flow in the
553   canopy layer on the wall pressure. Therefore, we emphasize on the necessity for more detailed
554   air flow measurements within the canopy layer to quantify both the effects of the small-scale
555   turbulent flow generated by the urban canopy and that of the large-scale turbulence owing to
556   the atmospheric air flow.

561 References:
562 [1] J. Hummelgaard, P. Juhl, K.O.Sæbjörnsson, G. Clausen, J. Toftum, G. Langkilde, Indoor
563 air quality and occupant satisfaction in five mechanically and four naturally ventilated
564 open-plan office buildings, Build. Environ. 42 (2007) 4051–4058.
565 [2] R. Marshall, A study of wind pressure on single-family dwelling in model and full scale, J.
566 Wind Eng. Ind. Aerodyn. 1 (1975) 177–199.
567 [3] M. Ohba, K. Irie, T. Kurabuchi, Study on airflow characteristics inside and outside a
568 cross-ventilation model, and ventilation flow rates using wind tunnel experiments, J. Wind
569 Eng. Ind. Aerodyn. 89 (2001) 1513–1524.
570 [4] J. Seifert, Y. Li, J. Axley, M. Rösler, Calculation of wind-driven cross ventilation in
571 buildings with large openings, J. Wind Eng. Ind. Aerodyn. 94 (2006) 925–947.
572 [5] O.S. Asfour, M.B. Gadi, A comparison between CFD and Network models for predicting
573 wind-driven ventilation in buildings, Build. Environ. 42 (2007) 4079–4085.
574 [6] J.I. Peren, T. van Hoof, B.C.C. Leite, B. Blocken, Impact of eaves on cross-ventilation of a
575 generic isolated leeward sawtooth roof building: Windward eaves, leeward eaves and eaves
576 inclination, Build. Environ. 92 (2015) 578–590.
577 [7] J.I. Peren, T. van Hoof, B.C.C. Leite, B. Blocken, CFD simulation of wind-driven upward
578 cross ventilation and its enhancement in long buildings: Impact of single-span versus
579 double-span leeward sawtooth roof and opening ratio, Build. Environ. 96 (2016) 142–156.
580 [8] H. Cheng, P. Hayden, A.G. Robins, I.P. Castro, Flow over cube arrays of different packing
581 densities, J. Wind Eng. Ind. Aerodyn. 95 (2007) 715–740.
582 [9] S.A. Zaki, H. Hagishima, J. Tanimoto, N. Ikegaya, Parameters of Urban Building Arrays
583 with Random Geometries, Bound.-Layer Meteorol. 138 (2011) 99–120.
584 [10] Y.C. Kim, A. Yoshida, Y. Tamura, Characteristics of surface wind pressure on low-rise
585 building located among large group of surrounding buildings, Eng. Struct. 35 (2012) 18–28.
586 [11] N. Ikegaya, C. Hirose, A. Hagishima, J. Tanimoto, Effect of turbulent flow on wall
587 pressure coefficients of block arrays within urban boundary layer, Build. Environ. 100 (2016)
588 28–39.
589 [12] J.O.P. Cheung, C.H. Liu, CFD simulations of natural ventilation behaviour in high-rise
590 buildings in regular and staggered arrangements at various spacings, Energy Build. 43 (2011)
591 1149–1158.
592 [13] Y. Murakami, N. Ikegaya, A. Hagishima, J. Tanimoto, Coupled simulations of
593 indoor-outdoor flow fields for cross-ventilation of a building in a simplified urban array,
594 Atmosphere 9(6) (2018) 217.
595 [14] Y. Tominaga, B. Bloken, Wind tunnel experiments on cross-ventilation flow of a generic
596 building with contaminant dispersion in unsheltered and sheltered conditions, Build. Environ.
597 92 (2015) 452-461.
598 [15] N. Ikegaya, S. Hasegawa, A. Hagishima, Time-resolved particle image velocimetry for
599 cross-ventilation flow of generic block sheltered by urban-like block arrays, Build. Environ.
600 147 (2019) 132-145.
601 [16] M. Kanda, Large-eddy simulations on the effects of surface geometry of building arrays
602 on turbulent organized structures, Bound.-Layer Meteorol. 118 (2006) 151–168.
603 [17] I.P. Castro, H. Cheng, R. Reynolds, Turbulence over urban-type roughness: Deductions
604 from wind-tunnel measurements, Bound.-Layer Meteorol. 118 (2006) 109–131.
605 [18] T. Michioka, A. Sato, H. Takimoto, M. Kanda, Large-Eddy Simulation for the

606 Mechanism of Pollutant Removal from a Two-Dimensional Street Canyon, Bound.-Layer
607 Meteorol. 138 (2011) 195–213.

608 [19] H. Gough, T. Sato, C. Halios, C.S.B. Grimmond, Z. Luo, J.F. Barlow, A. Robertson, R.
609 Hoxey, A. Quinn, Effects of variability of local winds on cross ventilation for a simplified
610 building within a full-scale asymmetric array: Overview of the Silsoe field campaign, J. Wind
611 Eng. Ind. Aerodyn. 175 (2018) 408–418.

612 [20] M.F. King, H.L. Gough, C. Halios, J.F. Barlow, A. Robertson, R. Hoxey, C.J. Noakes,
613 Investigating the influence of neighbouring structures on natural ventilation potential of a
614 full-scale cubical building using time-dependent CFD, J. Wind Eng. Ind. Aerodyn. 169 (2017)
615 265–279.

616 [21] H.L. Gough, M.-F. King, P. Nathan, C.S. Sue Grimmond, A.G. Robins, C.J. Noakes, Z.
617 Luo, J.F. Barlow, Influence of neighbouring structures on building façade pressures:
618 comparison between full-scale, wind-tunnel, CFD and practitioner guidelines, J. Wind Eng.
619 Ind. Aerodyn. 189 (2019) 22–33.

620 [22] A. Inagaki, M. Kanda, Turbulent flow similarity over an array of cubes in near-neutrally
621 stratified atmospheric flow, J. Fluid Mech. 615 (2008) 101–120.

622 [23] M. Kanda, T. Moriizumi, Momentum and heat transfer over urban-like surfaces,
623 Boundary-Layer Meteorol. 131 (2009) 385–401.

624 [24] A. Inagaki, M. Kanda, Organized structure of active turbulence over an array of cubes
625 within the logarithmic layer of atmospheric flow, Boundary-Layer Meteorol. 135 (2010) 209–
626 228.

627 [25] H. Takimoto, A. Sato, J.F. Barlow, R. Moriwaki, A. Inagaki, S. Onomura, M. Kanda,
628 Particle image velocimetry measurements of turbulent flow within outdoor and indoor urban
629 Scale Models and flushing Motions in urban canopy Layers, Boundary-Layer Meteorol. 140
630 (2011) 295–314.

631 [26] A. Hagishima, J. Tanimoto, K. Nagayama, S. Meno, Aerodynamic parameters of regular
632 arrays of rectangular blocks with various geometries, Boundary-Layer Meteorol. 132 (2009)
633 315–337.

634 [27] MacDonald R.W., Griffiths R.F., Hall D.J., An improved method for the estimation of
635 surface roughness of obstacle arrays, Atmos. Environ. 32 (1998) 1857–1864.

636 [28] W.H. Snyder, I.P. Castro, The critical Reynolds number for rough-wall boundary layers, J.
637 Wind Eng. Ind. Aerodyn. 90 (2002) 41–54.

638 [29] S.A. Zaki, H. Hagishima, J. Tanimoto, Experimental study of wind-induced ventilation in
639 urban building of cube arrays with various layouts, J. Wind Eng. Ind. Aerodyn. 103 (2012)
640 31–40.

641 [30] H. Cheng, I.A.N.P. Castro, Near wall flow over urban-like roughness, Bound.-Layer
642 Meteorol. 104 (2002) 229–259.

643 [31] C. Coceal, T.G. Thomas, I.P. Castro, S.E. Belcher, Mean flow and turbulence statistics
644 over groups of urban-like cubical obstacles, Bound.-Layer Meteorol. 121 (2006) 491–519.

645 [32] T.R. Oke, Boundary Layer Climates, 2nd edition (1987) 266–268.